Opto-mechanical design of a Bifocal Panoramic Lens for space applications

Davide Greggio[a], Paolo Martini[a], Emanuele Simioni[a], Oleksandra Rebrysh[a], Diego Scaccabarozzi[b], Marco Giovanni Corti[b], Alessandro Mulig De Palmenberg[b], Bortolino Saggin[c], Luigi Lessio[a], and Claudio Pernechele[a]

[a]Osservatorio Astronomico di Padova, Vicolo dell'Osservatorio 5, 35122 Padova, Italy
[b]Dipartimento di Meccanica, Politecnico di Milano, Polo Territoriale di Lecco, via G. Previati 1c, 23900, Lecco, Italy
[c]Dipartimento di Ingegneria Industriale, Università di Padova, Via Gradenigo 6/a, 35131, Padova, Italy

ABSTRACT

In this paper, we provide a detailed description of a bifocal panoramic lens (BPL), which allows recording a 360°x100° field and, simultaneously, a 20° circular field at a higher resolution. The BPL optical design has been specifically optimized for space environment operations. Furthermore, we describe the results of the tolerance and ghost analyses conducted on the camera, highlighting the challenges arising when dealing with such a wide-field objective due to entrance pupil aberrations and distortions.

Keywords: optical design, panoramic photography, ultra-wide angle lens, bifocal lens, tolerancing, ghost analysis, distortion

1. INTRODUCTION

Ultra-wide field imaging plays a crucial role in space and planetary observation and exploration. Traditionally, panoramic images can be reconstructed using cameras with a field of view typically limited to a few tens of degrees. This approach requires either changing the camera's pointing direction with movable elements or employing systems composed of multiple cameras, properly aligned and calibrated, to reconstruct the full panoramic scene. Both solutions are sub-optimal for space operations due to the presence of movable parts or because they are too heavy and bulky.

An alternative solution involves using ultra-wide FoV panoramic lenses.[1] In this paper, we present the design of a bifocal panoramic lens optimized for operation in space environments. This lens is capable of simultaneously recording, on the same detector, a panoramic FoV spanning the full 360° Azimuth range and several tens of degrees above and below the horizon, as well as a circular frontal FoV of 20° with higher resolution.

The capabilities of the bifocal panoramic lens have already been demonstrated in a ground application,[2] showing the versatility of such an optical configuration. More recently, bifocal panoramic lenses (BPLs) have gained significant interest in space applications, mainly due to their reduced weight, low power consumption, and absence of moving parts. For example, the use of BPL-based sensors for space applications has recently been funded for various purposes,[3] such as multi-purpose star trackers, immersive cameras for exploring lunar caves and lava tubes, planetary surface monitoring cameras, and lander exhaust plume monitoring.

One of the major drawbacks of panoramic lenses is their relatively low resolution due to the extremely large FoV being captured by a single detector. Despite this, panoramic lenses offer a viable solution for wide-field monitoring on space missions. This is because high resolution is already constrained by the limited bandwidth for data transfer to Earth, and recent advances in computational super-resolution may mitigate this issue.

Further author information:
D. Greggio: E-mail: davide.greggio@inaf.it
C. Pernechele: E-mail: claudio.pernechele@inaf.it

Space Telescopes and Instrumentation 2024: Optical, Infrared, and Millimeter Wave, edited by Laura E. Coyle, Shuji Matsuura, Marshall D. Perrin, Proc. of SPIE Vol. 13092, 130927J · © 2024 SPIE · 0277-786X · doi: 10.1117/12.3020431

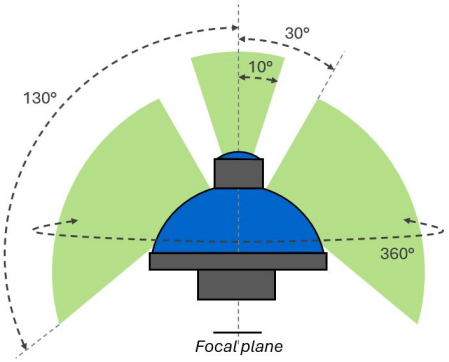

Figure 1. Field of view of the Bifocal Panoramic Lens

In this paper we focus on the optical design of a BPL dedicated to space missions. Since the BPL must adapt to various applications, the design optimization has been performed to meet general space requirements: 1) A temperature range without active control between -120°C and +120°C; 2) The use of radiation-hardened glasses; 3) Ensuring the first resonance is above 150 Hz to avoid resonances and withstand the excitation during launch.

2. OPTICAL DESIGN

To optimize the scientific and engineering return of the extremely large field of view of the panoramic lens, we conducted a trade-off analysis of available image sensors within the COTS (commercial off-the-shelf) space market. To sample the panoramic image with as many pixels as possible in the smallest possible sensor format, we selected the SONY Pregius IMX264 chip, which has a 2/3" format and a 2464 x 2056 px matrix (pixel size of 3.45 micrometers). This chip is mounted on a space qualified read-out electronic board by Imperx Ltd and is available as a COTS component up to 70 krad TID. The choice of this image sensor guided the subsequent optical design of the panoramic lens, ensuring that the panoramic image fits entirely within the 2/3" sensor format.

The lens has been optimized to work in visible light (from 485nm to 655 nm) and is based on a catadioptric design. All lenses directly exposed to the external environment are made of radiation-resistant optical glasses such as fused silica (L1) and BK7G18 (L4 and L5). Figure 2 shows the 2D optical layout of the lens, with ray-tracing of the frontal field (red rays) and the panoramic field (green rays). The most prominent optical element is a catadiopter (indicated as L5 in the figure) with a high curvature and a meniscus shape. The concave surface is reflective and, together with L4, serves to collect light beams from the panoramic field and reduce their speed. After this, the panoramic field light reaches the front surface of L3, which has a semi-reflective coating that reflects back half of the light and directs it towards the camera. The semi-reflective surface combines light from the frontal field with that of the panoramic field.

The frontal field, which is a cone with its axis pointing towards the zenith, enters the BPL from L1, reaches the semi-reflective surface of L3, and half of it is transmitted towards the detector while the other half is reflected back and lost. The concave surface of L5 is reflective only in the outer part, while the inner part is transmissive, allowing rays from L3 to reach the last group of lenses and be focused on the image plane. The panoramic field is imaged in a donut-shaped region on the detector with an inner radius of 1.22 mm and an outer radius of 3.4 mm. The frontal field is imaged in a circle with a radius of 1.12 mm. The aperture stop is placed between L7 and L8 and is common to both fields of view. The physical diameter of the stop is designed to produce an F/3.5 focus.

The way the 3D object space is mapped onto the 2D focal plane is described by the lens mapping equation depicted in the right plot of figure 2. The plot shows the real image height as a function of the input angular field from the optical axis. The function is highly non-linear for the panoramic field, indicating that the effective focal length changes with the field. Depending on the optical system, the mapping function can take different forms. For example, in the case of an equidistant projection, the relationship is linear, meaning that angular

distances are preserved in the image plane. In our case, the angular resolution measured at the image plane decreases from $0.027°/\mu m$ at zenith angles of 30° to $0.13°/\mu m$ at zenith angles of 130°. For the frontal field, instead, the projection is approximately equidistant, with a constant resolution of $0.5 arcmin/\mu m$.

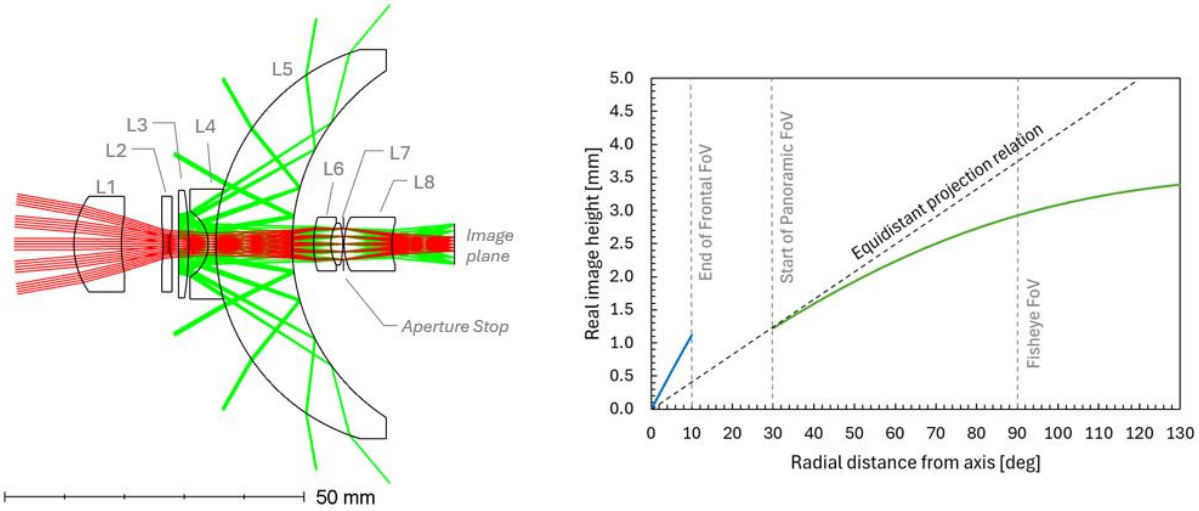

Figure 2. Left: 2D Optical layout of the Bifocal Panoramic Lens. Right: Lens mapping function for the frontal FoV (blue line) and the panoramic FoV (green line).

The image quality is evaluated in terms of RMS spot radius. For both the frontal and panoramic imaging channels, optical aberrations are well corrected, as shown in the spot diagram in figure 3. The nominal RMS spot radius is approximately $2.0\mu m$ over the entire FoV, except the very edges of the field where it reaches $4.3\mu m$. In the figure, we also include the size of the Airy diffraction disk as a black circle for comparison.

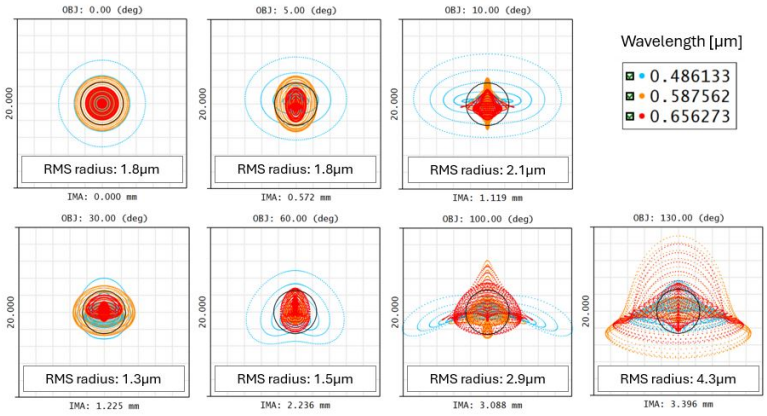

Figure 3. Spot diagrams for the frontal FoV (top) and the panoramic FoV (bottom). The black circles represent the size of the Airy disc at the mid wavelength.

Another typical feature of ultra-wide field lenses is that the entrance pupil position changes as a function of the field. The entrance pupil area also varies with the field, generally decreasing as the entrance angle of the rays increases. To properly account for these effects, ray-tracing software includes algorithms to optimize the starting position of rays so that they will enter the pupil stop. In our case, we modeled the system using Zemax OpticStudio with the "robust real-ray aiming" feature for the panoramic field. This feature is essential to avoid ray-tracing errors, but as we will see later, it is not sufficient when accounting for manufacturing and alignment

errors because the algorithm used for optimizing the starting position of rays is unable to converge. Despite this limitation, which will be further analyzed in section 5, we can evaluate the effective entrance pupil area of the nominal design as a function of the radial field by calculating the footprint of the entrance beams projected onto a plane perpendicular to the chief ray. Figure 4 shows a schematic representation of the entrance pupil projection for three different field directions: A, B and C. The entrance pupil area as a function of the entrance angle, normalized by the maximum area of the field at 30° from the optical axis, is shown in the right plot of figure 4. For the edge field at 130° from the axis, the effective entrance pupil area is about 28% of the area at 30°. Such a feature should be considered for any radiometric analysis, along with the angular-dependent effects due to the coatings and the projection onto the image plane.

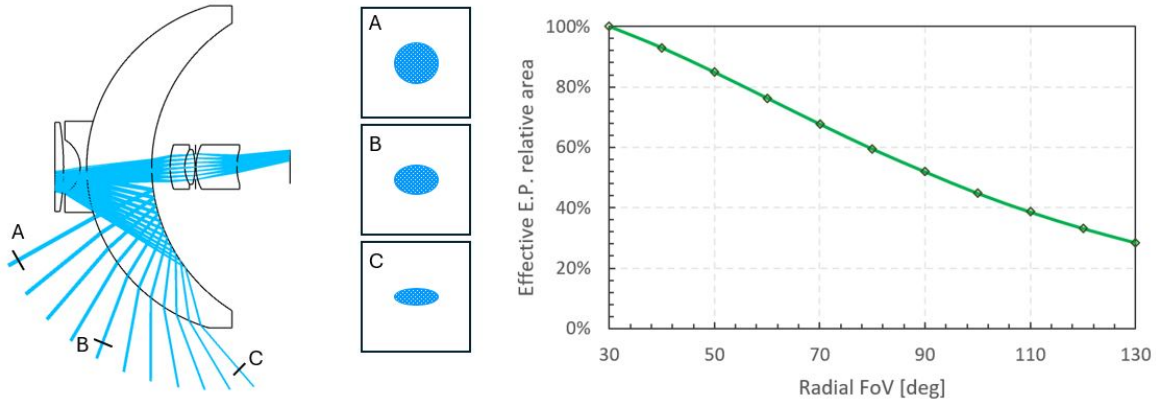

Figure 4. Left: schematic representation of the entrance pupil distortion of the BPL for three different directions A, B and C of the panoramic FoV. Right: normalized relative entrance pupil area as a function of the radial FoV for the panoramic field.

3. PASSIVE ATHERMALIZATION

After the design optimization, based on image quality and manufacturability criteria, we assessed the thermal behavior of the objective. The analysis was conducted using the Zemax multiple-configuration feature, modeling thermal contraction or expansion through a linear approach based on the coefficient of thermal expansion (CTE) of the materials. The temperature dependence of the refractive index is derived from catalogue data provided by the program. The temperature of the system is assumed to be uniform without any thermal gradient.

We initiated the evaluation with the panoramic channel, assuming the mechanical spacers between the lenses were made of titanium ($CTE = 9 \cdot 10^{-6}\ [^{\circ}C]^{-1}$). Subsequently, we optimized the CTE of the spacer between the objective and the detector to minimize thermal defocus within a temperature range of -120°C to +120°C. The optimal performance was achieved with a CTE of $37 \cdot 10^{-6}\ [^{\circ}C]^{-1}$. Next, we applied the same thermal model to the frontal field and checked the behavior of the thermal defocus. Figure 5 shows the variation of the RMS spot radius for several field points (different colors) as a function of the temperature. The panoramic field, for which the thermal defocus is well corrected, shows an almost constant spot size. The frontal fields, on the other hand, exhibit some temperature-dependent focus variation. However, the variation in the RMS spot radius is quite small considering the very wide temperature range. To better correct the focus term in the frontal field, a material with slightly lower CTE could be selected (approximately $CTE = 25 \cdot 10^{-6}\ [^{\circ}C]^{-1}$), at the expense of greater defocus for the panoramic field. As an alternative, it is possible to optimize the spacers between L1, L2 and L3, but we leave this work for a later design stage.

Even if a complete Finite Element (FE) analysis will be necessary in the future to validate these preliminary thermal results, a FE simulation has already been performed for the bonded optical group composed of L6 and L7. To ensure that deformations due to the different CTEs of the glasses do not cause a failure of the bonding or a breakage of one of the lenses within the full operational temperature range, we calculated that the difference

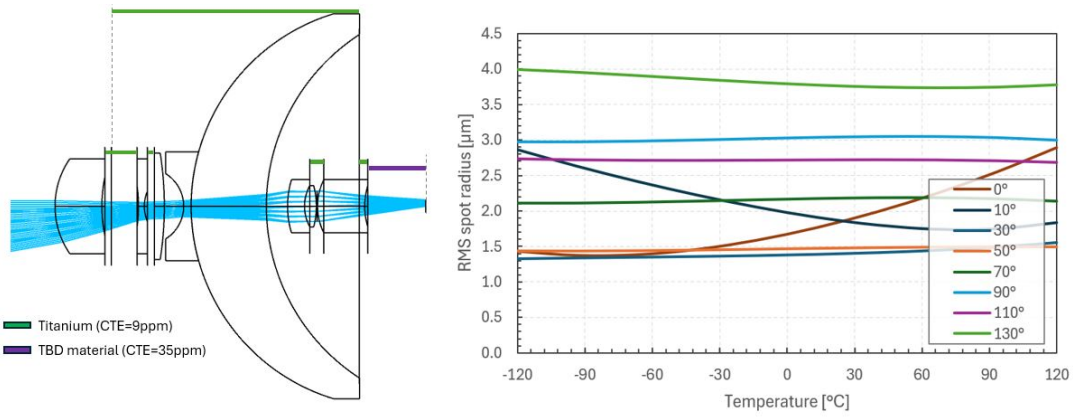

Figure 5. Left: schematic representation of the spacers between lenses. Green bars represent titanium spacers, the purple bar is a material still to be defined, with CTE possibly close to $37 \cdot 10^{-6}$ $[^{\circ}C]^{-1}$. Right: RMS spot radius as a function of the temperature for different field positions.

in CTE should be less than $0.6 \cdot 10^{-6}$ $[^{\circ}C]^{-1}$. The actual difference of the CTE of the S-TIH57 and N-LAK12 glasses is only $\Delta CTE = 0.1 \cdot 10^{-6}$ $[^{\circ}C]^{-1}$, well within the requirement.

4. THERMO-MECHANICAL DESIGN

In the thermo-mechanical design of the supporting structure for the BPL, the holder for the catadioptric lens is one of the most critical parts of the assembly since this lens has the largest size and mass of the instrument. Among the possible solutions, gluing the catadioptric lens to the mechanical group holding lenses L1, L2, and L3 was suggested to exploit the full FoV of the optical system without limiting its performance.

Gluing optics to a metal frame is challenging due to the high stresses that arise when different materials are bonded together and subjected to thermal cycling, especially without any active thermal control system. Even a small mismatch of the CTEs can cause stresses at the interface, leading to cracks in the optics and, consequently, performance degradation or mission failure. Additionally, the mechanical environment is critical due to the high vibration levels expected at launch, especially the random vibration levels from the rocket liftoff.

These considerations guided the design solution, suggesting the use of an intermediate material, softer than the optics and holder materials, to accommodate the CTE mismatch over a large temperature range. The design requires a trade-off between the thermal compliance of the supporting structures within the working temperature range, their mechanical resistance to high levels of loading from the mechanical environment, and instrument performance. The proposed solution uses intermediate pads made of high-performance plastics (e.g., Torlon 7130 and CFP materials) between the catadioptric lens and the mechanical holder. The material and geometry of the pads and the holder are under development to meet the design requirements.

Figure 6 shows the developed finite element model used to evaluate the thermo-elastic stress distribution at the interface with the catadioptric lens. It can be seen that the stress is in the range of 15 MPa at the glass interface, providing a safety margin of about 3 with respect to the 50 MPa threshold. Additional analyses are underway to evaluate the increase in stress due to the compliant flexure of the holder, which is required to withstand the mechanical loading of the intended application. Moreover, testing activities on samples to reproduce the bonding at the interface are planned to obtain experimental validation of the proposed solution. This latter activity is particularly important because the CTEs of the materials used are only partially known within the working temperature range.

5. TOLERANCE ANALYSIS

To preserve optical quality and guide manufacturing and alignment processes, we conducted a tolerance analysis. We employed a standard method involving an initial sensitivity analysis followed by a Monte Carlo simulation

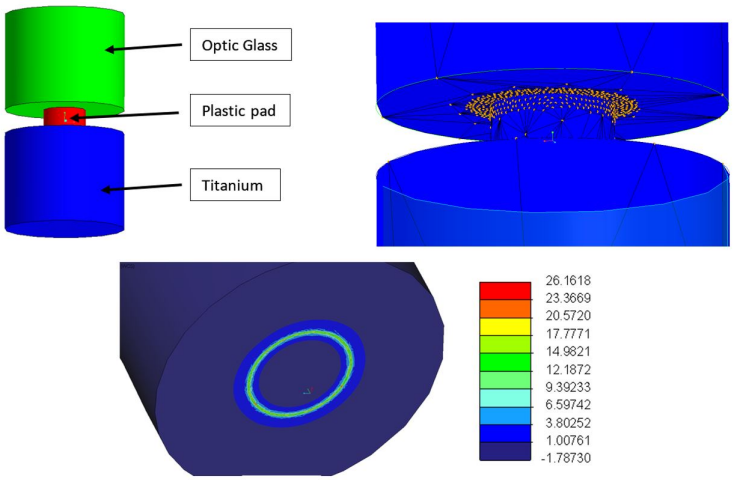

Figure 6. Left: Finite Element (FE) model for the thermal stress distribution at the interface between pad and optics. Center: meshed model. Right: Max principal stress state – Torlon 7130 pad / glass interface (units MPa).

with 1000 random realizations, using a parabolic distribution of errors to ensure statistical significance. The only compensator used was the distance between L8 and the image plane to refocus the system. We established tolerances for both panoramic and frontal fields. For common-path elements, we selected the configuration with the strictest tolerance as the final requirement.

During the Monte Carlo simulation of the panoramic field, we encountered ray-tracing errors arising from the inability of the ray aiming algorithm to properly calculate starting rays. To address this, we manually defined each field, specifying the entrance pupil offset and vignetting factors. We intentionally oversized the illuminating beam diameter for each field by a factor of 2-3 relative to the pupil stop size. While this results in sub-optimal pupil sampling, with many rays falling outside the pupil aperture and being vignetted, it ensures that the beam illuminates the stop even when considering tolerances. This allows for accurate spot diagram calculations provided a sufficient pupil grid sampling is used (we employed a 40x40 rays grid sampling).

The resulting tolerances are reported in tables 1 and 2. Generally, the panoramic field is less tolerant than the frontal one, but no critical issues were identified. Considering the worst RMS spot radius across the field of view (FoV) as the image quality criterion, the 98th percentile of the Monte Carlo distribution is characterized by an enlargement of the spot radius of approximately $1\mu m$ both for the frontal and the panoramic fields.

6. GHOST ANALYSIS

The ghost analysis is based on non-sequential ray-tracing simulations. The source is placed at infinity and illuminates the full camera at angles ranging from 0° to 160° in 5° increments. For each angle, all the rays hitting the detector are recorded, and ghost paths are analyzed using appropriate filtering.

A second analysis was performed using backward ray-tracing from the detector. A 7x7 mm rectangular source emitting rays in a cone with a 25° angular extension from the optical axis was used to estimate the irradiance distribution on a spherical detector centered on the camera objective. The radius of the spherical detector was set to 1000 mm, significantly greater than the physical size of the objective. This setup ensures that the positions of the rays recorded by the detector approximate the angular distribution of the rays exiting the objective. The rays are uniformly distributed over the detector area and uniformly distributed in the angular direction with which they are generated. The irradiance distribution on the spherical detector thus represents the throughput of the optical system as a function of the polar and azimuthal angles.

For the coatings we made the following working assumptions:

Table 1. Alignment tolerances for the frontal (black) and panoramic (red) fields.

	Glass	Decenter [mm]	Tilt [deg]	Axial distance to next element [mm]
L1	Fused silica	±0.200	±0.500	±0.100
L2	N-PK51	±0.040	±0.300	±0.100
L3	N-SF6	±0.200 / ±0.200	±0.500 / ±0.070	±0.100 / ±0.015
L4/L5 Group	BK7G18 / BK7G18	±0.030 / ±0.005	±0.080 / ±0.080	±0.100 / ±0.050
L6/L7 Group	S-TIH57 / N-LAK12	±0.020 / ±0.004	±0.130 / ±0.050	±0.100 / ±0.070
STOP	-	±0.070	±0.500	±0.100 / ±0.080
L8	N-LAK33B	±0.030 / ±0.010	±0.120 / ±0.040	*
Image plane	-	±0.100	±0.150	-

* Used as compensator

Table 2. Manufacturing tolerances for the frontal (black) and panoramic (red) fields.

		Glass	RoC tolerance [fringes]	Central thickness [mm]	Wedge [arcmin]	Irregularity [fringes]	Refractive index	Abbe number
L1	**L1S1**	Fused silica	±5	±0.150	9.1	±2	±1e-3	±0.5
	L1S2		±5			±2		
L2	**L2S1**	N-PK51	±5	±0.150	24.6	±2	±1e-3	±0.5
	L2S2		±5			±2		
L3	**L3S1**	N-SF6	±5 / ±3	±0.150 / ±0.030	13.7 / 7.2	±2 / ±1	±1e-3 / ±1e-3	±0.2 / ±0.2
	L3S2		±5 / ±5			±2 / ±1		
L4	**L4S1**	BK7G18	±5 / ±5	±0.150 / ±0.040	15.7 / 3.6	±2 / ±2	±1e-3 / ±1e-3	±0.5 / ±0.5
	L4S2		±5 / ±5			±2 / ±2		
L5	**L5S1**	BK7G18	±5 / ±5	±0.150 / ±0.150	7.6 / 2.4	±2 / ±2	±1e-3 / ±5e-4	±0.5 / ±0.5
	L5S2		±5 / ±5			±1.5 / ±1		
L6	**L6S1**	S-TIH57	±5 / ±5	±0.150 / ±0.150	1.7 / 1.3	±1 / ±0.7	±1e-3 / ±1e-3	±0.2 / ±0.2
	L6S2		±5 / ±5			±1.5 / ±1		
L7	**L7S1**	N-LAK12	±5 / ±5	±0.080 / ±0.100	3.4 / 1.3	±2 / ±2	±1e-3 / ±7e-4	±0.4 / ±0.4
	L7S2		±5 / ±3			±1 / ±0.7		
L8	**L8S1**	N-LAK33B	±5 / ±5	±0.150 / ±0.050	10.1 / 8.4	±1.5 / ±1	±1e-3 / ±1e-3	±0.4 / ±0.4
	L8S2		±5 / ±5			±2 / ±1.5		

- The anti-reflection (AR) coating is assumed to be a COTS coating with reflectivity $< 0.5\%$ in the working waveband;
- the half-reflective plate is simulated as an ideal coating with 50% reflectivity and 50% transmission;
- the catadiopter mirror surface is assumed to be 100% reflective;
- all the side faces of the lenses are 100% absorbing.

In figure 7 we report the ratio between the maximum ghost irradiance and the image irradiance for every angle of incidence up to 130°. The highest irradiance ratio occurs at illumination angles between 30° and 50°.

This illumination range is dominated by a first-order ghost path, as shown on the right side of figure 7. The light experiences a ghost reflection on the first surface of the catadioptric lens and is reflected a second time by the reflective face of the catadioptric lens itself. After this, it follows the nominal imaging path and reaches focus very close to the detector. Since the ghost image originates from a single spurious reflection and is almost in focus, its irradiance is quite high and potentially troublesome. Unfortunately, it was not possible to eliminate this ghost path through design optimization while considering the other design constraints.

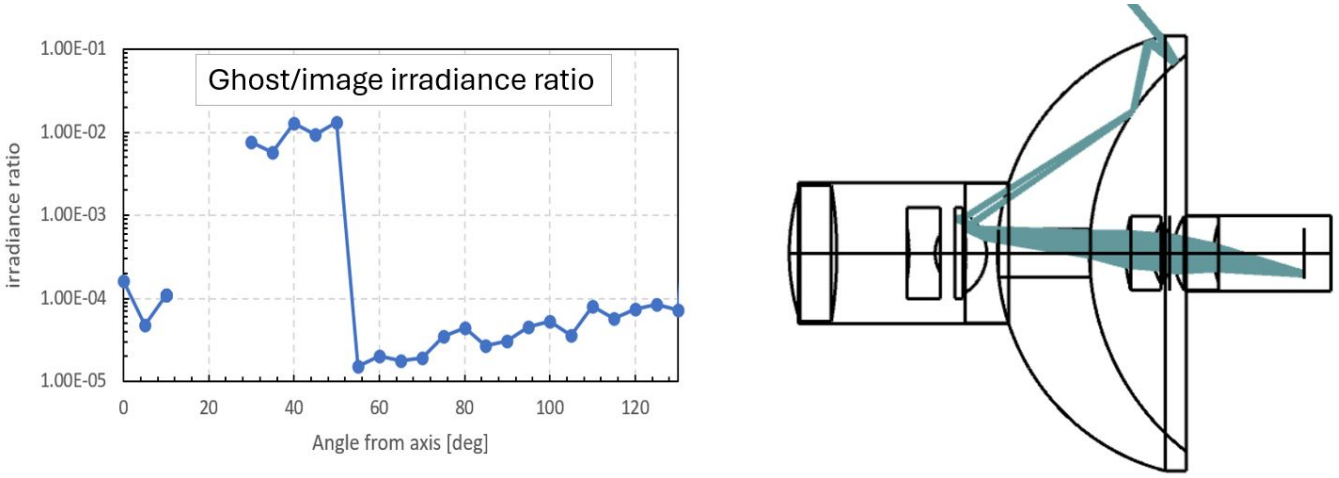

Figure 7. Left: ratio between the maximum ghost irradiance and the image irradiance as a function of the illumination angle from the optical axis. Right: optical path producing the highest irradiance ghost, at an illumination angle of 45°. The rays entering the catadiopter are ghost-reflected by the first surface of L5 and experience a second reflection from the second surface of L5.

The backward ray-tracing did not reveal any particular issues and confirmed that the effective FoV of the BPL coincides with the one used during design optimization. It also confirmed the decrease in system throughput as a function of the elevation angle, as previously calculated in figure 4.

7. CONCLUSIONS

The development of the Bifocal Panoramic Lens (BPL) for space applications addressed a series of complex design challenges and optimisation requirements. Through a careful design process, we have created a lens system that meets the necessary criteria for its intended use in space exploration.

The optical design was optimised to ensure high image quality across a wide field of view. Thermal analysis and passive athermalisation strategies were implemented to ensure the lens system remains functional across a broad temperature range typical of diverse space environments. Moreover, the thermo-mechanical design has been optimised to ensure the structural integrity of the lens system under varying thermal and mechanical loads. High-performance plastic intermediate pads between the catadioptric lens and its holder were used to accommodate CTE mismatches, thus preventing mechanical failure.

A tolerance analysis was conducted to assess the manufacturing and alignment sensitivities. Monte Carlo simulations confirmed that the system could maintain high image quality despite the tolerances, with no critical issues identified for both panoramic and frontal fields.

Finally, the ghost analysis verified the presence of some high-irradiance ghosts when the BPL is illuminated at angles between 30° and 50° from the axis. The presence of ghosts can be expected due to the extremely wide field of view for two main reasons: 1) the requirement to have an unvignetted field of view spanning such a wide angular range prevents the possibility of designing proper baffling, and 2) there is a higher probability of having bright sources in some directions of the field. These ghost images should be considered by the image acquisition and analysis system, especially when a bright source is present within this critical illumination angular range.

Currently, some prototyping activity is ongoing with the purpose of performing further performance and thermo-mecanical tests on a real model.

ACKNOWLEDGMENTS

We aknowledge Daniele Mura of 'Lobre S.R.L' for his precious technical support and feedback on the feasibility of the lenses.

This work is funded by ESA AO/2-xxx/20/NL/GLC, proposal TA 2-1739 OSIP Lunar Caves System Studies.

REFERENCES

[1] Pernechele, C., [*Introduction to Panoramic Lenses*], SPIE Digital Library, Bellingham, Washington (2018).

[2] Pernechele, C., "Hyper-hemispheric and bifocal panoramic lenses," in [*Electro-Optical and Infrared Systems: Technology and Applications X*], Huckridge, D. A. and Ebert, R., eds., **8896**, 889603, International Society for Optics and Photonics, SPIE (2013).

[3] C. Pernechele, P. Martini, E. S., "Omnidirectional panoramic lens applications," in [*Optics, Photonics and Laser: Proceedings of the 7th International Conference on Optics, Photonics and Lasers (OPAL 2024)*], 34–38 (05 2024).